Nanoscale chemistry of Zircaloy-2 exposed to three and nine annual cycles of boiling water reactor operation — an atom probe tomography study

(article starts on next page)

Nanoscale chemistry of Zircaloy-2 exposed to three and nine annual cycles of boiling water reactor operation — an atom probe tomography study

J. Eriksson[a,*], G. Sundell[a,1], P. Tejland[b], H.-O. Andrén[a], M. Thuvander[a]
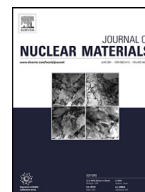
[a] *Dept. of Physics, Chalmers University of Technology, SE-412 96 Gothenburg, Sweden*
[b] *Studsvik Nuclear AB, SE-611 82 Nyköping, Sweden*

ABSTRACT

Atom probe tomography was used in this work to study the metal close to the metal/oxide interface in the zirconium alloy Zircaloy-2 exposed to three and nine annual cycles of operation in a commercial boiling water reactor. The two exposure times correspond to before and after the onset of acceleration in corrosion, hydrogen pickup, and growth.

The alloying elements Sn, Fe, Cr, and Ni were observed to be redistributed after exposure. After both three and nine cycles, clusters containing Fe and Cr and typically of a spheroidal shape with an approximate diameter of 5 nm were observed to be located in layers presumed to be layers of $<a>$-loops. On average, the cluster number density was slightly higher after nine cycles, with larger and more Cr-rich clusters. However, there were large grain-to-grain variations, which were larger than the differences between the two exposure times. Ni was only occasionally observed in the clusters. Sn was observed to be slightly enriched in the Fe–Cr clusters, but the Sn concentration was higher between than inside the layers of clusters. After nine cycles, clusters of Sn were detected in regions that were depleted of Fe and Cr. Enrichment of Sn, Fe, and Ni at features that appeared to be $<c>$-component loops was observed after nine cycles, whereas no such features were observed after three cycles. Enrichment of Sn and Fe, and small amounts of Cr and Ni, was observed at grain boundaries after both exposure times. After three cycles, a partially dissolved second phase particle of $Zr(Fe,Cr)_2$ type that contained about ten times more Cr than Fe was observed.

© 2022 The Author(s). Published by Elsevier B.V.
This is an open access article under the CC BY license (http://creativecommons.org/licenses/by/4.0/)

1. Introduction

Zirconium alloys are used in nuclear reactors as structural core components and as cladding tubes for the nuclear fuel. The alloy Zircaloy-2, which contains Sn, Fe, Cr, Ni, and O as alloying elements, is commonly used in boiling water reactors (BWRs). As the solubility of Fe, Cr, and Ni in the matrix is very low [1–6], these elements are in the as-produced material located in second phase particles (SPPs) of the two types $Zr(Fe,Cr)_2$ and $Zr_2(Fe,Ni)$, whereas Sn and O are in solid solution in the matrix [7]. The two types of SPPs are usually separate from each other, but sometimes $Zr(Fe,Cr)_2$ and $Zr_2(Fe,Ni)$ SPPs can form adjacent to each other, creating an SPP with one Fe-Ni-rich part and one or a few Fe–Cr-rich parts [8–10]. When exposed to the neutron flux in the reactor, the SPPs start to dissolve, releasing Fe, Cr, and Ni into the matrix [9–13]. It has been observed that Fe is released before Cr from dissolving $Zr(Fe,Cr)_2$ SPPs and that the $Zr_2(Fe,Ni)$ SPPs dissolve later than the $Zr(Fe,Cr)_2$ SPPs [9,10,13].

Zr alloys have hexagonal close-packed (HCP) structure. When they are irradiated by neutrons, small dislocation loops are formed in the matrix [14]. The dislocation loops can be of $<a>$-type, having Burgers vector only in the $<a>$-directions, or of $<c>$-component type, having Burgers vector with a component in the $<c>$-direction [14]. In neutron-irradiated Zr and Zr alloys, $<a>$-loops form already after low fluence, whereas $<c>$-component loops have been observed only after high fluence [14]. The habit plane of the $<a>$-loops is close to, but usually not exactly on, one of the first-order prismatic planes [15,16], and $<a>$-loops align in layers that are parallel to the basal planes of the matrix [16]. The $<c>$-component loops are found on the basal planes [17–19]. Interstitial and vacancy $<a>$-loops have been reported to co-exist

---

* Corresponding author.
E-mail address: ejoha@chalmers.se (J. Eriksson).
[1] Now at Vitroprobe Analytics AB, Danska vägen 83, SE-416 59 Gothenburg, Sweden

in neutron-irradiated Zr and Zr alloys [14,16,18], whereas $<c>$-component loops have been observed only as vacancy-type loops [14,17,18]. In neutron-irradiated Zircaloy-2, transmission electron microscopy (TEM) observations have revealed typical $<a>$-loop sizes of up to 10 nm [20,21] and typical $<c>$-component loop sizes around 100 nm [21].

In Zircaloy-2 exposed to reactor operation, the alloying elements have been observed to cluster at confirmed or assumed positions of dislocation loops [10,21–26]. Using atom probe tomography (APT), Sundell et al. observed clusters of Fe and Cr, sometimes with very small amounts of Ni, aligned in the typical way of $<a>$-loops [22]. Also clustering of Sn was observed, but only in regions where the concentration of Fe, Cr, and Ni was very low. Furthermore, segregation of Fe and Sn to ring-shaped features, interpreted to be small $<c>$-component loops, was observed. In a TEM study by Harte et al., clusters consisting mainly of Fe and Cr or mainly of Fe and Ni at positions of $<a>$-loops were observed [21]. An observation of anticorrelation between layers of high Sn concentration and layers of Fe–Ni clusters was also made. Using APT and TEM, Sawabe and Sonoda observed that clusters of Fe and Cr were located close to partially dissolved $Zr(Fe,Cr)_2$ SPPs and close to grain boundaries (GBs), whereas clusters of Fe but not Cr were located in the matrix further away from these features [23]. In an APT study by Cockeram et al., observations of clustering of Sn, Fe, Cr, and, in a few cases, Ni were made [24]. Their observed cluster number density was higher close to SPPs than further away in the matrix. In an APT and TEM study, Jenkins et al. observed that there was a network-like structure of Sn within the layers of Fe–Cr clusters, that the clusters were located along this network, and that it connected to the Sn-rich regions between the layers of clusters [26]. In contrast to the other studies [21–23], which were performed on materials that had been exposed to commercial BWR operation, the studies of Cockeram et al. [24] and Jenkins et al. [26] were performed on materials that had been irradiated in test reactors, where the neutron flux is higher.

In another APT study of Zircaloy-2 exposed to commercial BWR operation, we observed a difference in morphology between clusters of Fe and Cr and clusters of Fe and Ni such that Fe–Cr clusters appeared spheroidal, as in [22] and [23], whereas Fe–Ni clusters appeared disc-shaped [25]. In [25], which presents results from an Ni-rich region close to the metal/oxide interface, a larger number density of Fe–Ni clusters than Fe–Cr clusters was observed. Furthermore, the disc-shaped Fe–Ni clusters were observed to be located at planes corresponding to first-order prismatic planes, but with a tilt away from the $<c>$-direction. This arrangement of $<a>$-loops is similar to previous TEM observations [15,16,27] and to results of molecular dynamics (MD) simulations [28]. The shape of the clusters in [24] and the Fe–Ni clusters in [25] matches what has been predicted in MD and Monte Carlo (MC) simulations of segregation of Fe and Ni to $<a>$-loops [29,30], but the shape of the Fe–Cr clusters observed in [22,23,25] does not match this predicted segregation.

During reactor operation, Zr alloys are degraded by corrosion [31] and hydrogen pickup (HPU) [32]. They also undergo irradiation-induced growth [33]. These phenomena limit the lifetime of the fuel rods, which typically are replaced after around five years in a BWR. It is highly desired to increase the lifetime of the fuel rods, thereby allowing for more efficient use of the nuclear fuel. Therefore, it is of interest to better understand the link between the chemical evolution of the material on a nanoscale and its corrosion, HPU, and growth, as it is known that alloying elements and impurities affect these processes [33–35]. Results from APT studies of local chemistry in the metal close to the metal/oxide interface in Zircaloy-2 exposed to long-term operation (nine annual cycles) in a commercial BWR have previously been published by us [22,25]. In the present study, APT observations of this material

with a shorter exposure time of three annual cycles are presented and compared with results, both previously published and unpublished, after nine cycles, providing information about the irradiated microstructure and its chemistry before and after the onset of acceleration in corrosion, HPU, and growth. General observations are presented, as well as information on bulk and matrix chemistry, an investigation of Fe–Cr clusters, observations regarding the distribution and clustering of Sn, enrichment of alloying elements at GBs, and the distribution of elements (including hydrogen) inside and outside a partially dissolved SPP.

2. Material

The material studied was the same as that investigated by Sundell et al. [22], i.e. LK3-type Zircaloy-2 cladding supplied by Westinghouse. Prior to analysis, the material had been exposed to either three annual cycles (3C) or nine annual cycles (9C) of reactor operation in a commercial BWR at Kernkraftwerk Leibstadt in Switzerland. Material of the same type exposed to three, five, six, seven, or nine cycles in the same reactor has been studied in [9,10,13,21,22,25,36–53]. The 3C sample had been exposed to a fast neutron fluence ($E > 1$ MeV) of 7.4×10^{25} n m^{-2}. It was taken out at an elevation of 2030–2350 mm from the bottom of rod AEB070-E4-N, for which the average burnup was 34.7 MWd/kgU, the oxide thickness 5 ± 2 μm, and the average hydrogen content 44 ± 2 wt ppm (corresponding to 0.4 at.%) [13]. The 9C sample had been exposed to a fast neutron fluence ($E > 1$ MeV) of 16.5×10^{25} n m^{-2}. It was taken out at an elevation of 1218–1308 mm from the bottom of rod AGB108-G6, for which the average burnup was 78.7 MWd/kgU, the oxide thickness 45 ± 7 μm, and the average hydrogen content 664 ± 94 wt ppm (roughly corresponding to 6 at.%) [13]. Hence, the oxide was about 9 times thicker and the HPU was 15 times higher than after 3C, indicating that accelerated corrosion and HPU had occurred in the 9C sample. Using the conversion factor for BWRs in [54], the fluence of the 3C and 9C samples corresponds to 11.9 and 26.5 dpa, respectively. The content of alloying elements and the impurities Si and N in the material is shown in Table 1.

3. Experimental

The experimental procedure was the same as that described by Sundell et al. [22]. Atom probe specimens were prepared at the hotlab of Studsvik Nuclear AB, using the focused ion beam–scanning electron microscopy (FIB–SEM) lift-out technique [55]. The lift-outs were done in the Zr metal, approximately 0–5 μm from the metal/oxide interface. An APT instrument of the type Imago LEAP 3000X HR with a detection efficiency of 0.37 was used for the measurements. Laser pulsing with a green laser ($\lambda = 532$ nm) with pulse energy in the range 0.25–0.50 nJ and pulse frequency at 50–250 kHz was used. The specimen temperature was in the range 20–80 K. In addition to the 15 APT analyses of the 9C sample reported by Sundell et al. [22], six APT analyses of the 3C sample were made.

Data evaluation was performed using the Cameca software IVAS 3.6.14. Bulk compositions (including the whole reconstructed volume, with GBs and clusters but not SPPs) and matrix compositions (excluding GBs, clusters, and SPPs) were calculated using peak decomposition with divalent Sn ions (the only charge state detected for Sn), monovalent and divalent Fe and Cr ions, and divalent Ni ions (as the severe overlaps between Ni$^+$ and Sn^{2+} were not possible to reliably decompose). The necessity to use only Ni^{2+}, which generally requires a higher field strength than Fe^{2+} and Cr^{2+} to be formed [56], might have led to an underestimation of the Ni content. However, this should not severely affect the comparison of the 3C with the 9C specimens. For the matrix compositions,

Fe–Cr clusters were excluded using isoconcentration surfaces. The elements H, C, O, and Ga (from the specimen preparation in the FIB) were excluded from the composition analysis. For analysis of Fe–Cr clusters, regions of interest (ROIs) were chosen from three APT reconstructions of the 3C specimens and from six APT reconstructions of the 9C specimens. The choice of ROIs was adapted to individual grains (excluding GBs) encountered in the analyses, and regions that appeared to be damaged by Ga from ion milling during specimen preparation in the FIB were excluded from the ROIs. Cluster analysis was performed using the maximum separation method (MSM) [57,58], with the following values of the parameters: $d_{max} = 1.2$ nm, $L = d_{max} = d_{erosion}$, $N_{min} = 10$, and order 1 for clusters consisting of Fe and/or Cr. Divalent Fe and Cr ions were used to define the clusters. The ratio Fe/(Fe+Cr) and the number of Fe and Cr atoms for each individual cluster were calculated using the values from MSM, whereas the average values for all clusters in each evaluated grain were calculated including both monovalent and divalent Fe and Cr ions and using peak decomposition. Clusters of Sn in two ROIs in APT reconstructions of the 9C specimens were defined by divalent Sn ions and investigated using the following values of the MSM parameters: $d_{max} = 0.8$ nm, $L = d_{max} = d_{erosion}$, $N_{min} = 10$, and order 1. The average number of Sn atoms per cluster was calculated using peak decomposition.

It is known that hydrogen redistribution and hydride formation can occur during sample and specimen preparation, e.g. in the FIB [59,60], and that H in the mass spectrum can result from the residual gas in the analysis chamber of the APT instrument [61,62]. Therefore, the H content, which in the 3C specimens was similar to that previously reported for the 9C specimens (20–66 at.%) [22], was not analysed further, with the exception of one specimen containing a partially dissolved SPP, where the H content inside and outside the SPP was measured. This was done to compare with other measurements of H in and around SPPs in as-produced and in autoclave-exposed material.

4. Results

4.1. General observations

The APT reconstructions of 3C and 9C specimens look similar, with large grain-to-grain variations and large variations within individual grains after both exposure times. To visibly distinguish the reconstructions of 3C from 9C is generally not possible. Spheroidal clusters, typically about 5 nm in diameter and containing Fe and Cr but generally not Ni, were observed in most of the specimens. After 9C, some Cr-rich clusters were observed to be larger and have a shape that was not spheroidal. Two other notable visual differences between the two exposure times are ring-shaped features, interpreted to be small <c>-component loops, observed in four of the 9C specimens and regions with Sn clusters observed in two of the 9C specimens. None of these features were observed in any of the 3C specimens. Fig. 1 shows the reconstructions of two 3C specimens and one 9C specimen. More figures showing reconstructions of 9C specimens can be found in [22]. Many features that (based on changes in orientation of layers of clusters and on segregation of alloying elements) appear to be GBs were observed. The number density of these GBs, which is much higher than in as-produced LK3-type Zircaloy-2 (grain size of about 4 µm), strongly
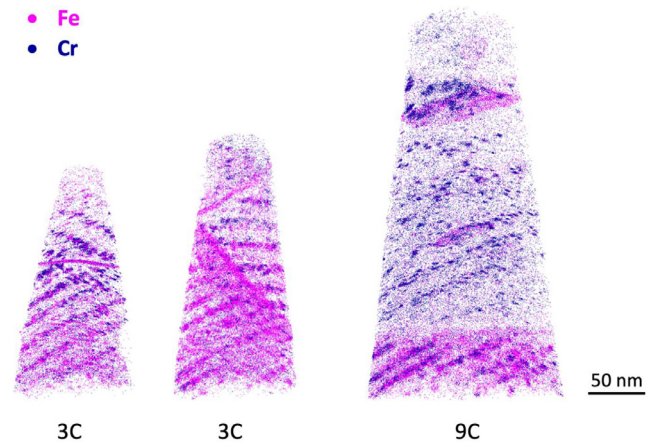

Fig. 1. Distribution of Fe and Cr atoms in the APT reconstructions of two of the 3C and one of the 9C specimens. Clusters of Fe and Cr are aligned in layers that are perpendicular to the <c>-direction in each grain.

indicates that they are subgrain boundaries (sub-GBs) that were created close to the metal/oxide interface during the growth of the oxide, as observed in [63]. Enrichment of Sn and Fe and small amounts of Cr and Ni at the GBs was observed after both 3C and 9C. In a majority of the specimens where one or more GBs were detected, large Cr-rich clusters were preferentially located close to the GBs, in agreement with the observations by Sawabe and Sonoda [23].

The observed clusters of Fe and Cr, both after 3C and 9C, were aligned in layers parallel to the basal planes of the Zr matrix, as observed in previous APT and TEM studies [21–23]. This could be verified, since in some of the grains the (0001) pole was observed on the ion density map, and at this pole Zr atoms were visible on crystallographic planes perpendicular to the pole, similarly to what is reported in [25]. The clusters are therefore most likely related to <a>-loops. There are large variations between the observed grains regarding Fe and Cr content. Some grains are Fe rich, some are Cr rich, and some contain Fe and Cr in about equal amounts. Furthermore, there are grains and regions of grains that contain almost no clusters of Fe and Cr. One example of a layer of clusters from a 3C specimen and one example of a layer of clusters from a 9C specimen are shown in Fig. 2. Both layers are viewed in the approximate <c>-direction. The layer from the 3C specimen was from the lower grain in the reconstruction to the left in Fig. 1, and the left part of the layer (as shown in Fig. 2) was close to the GB in Fig. 1. The layer from the 9C specimen was located about 100–150 nm from an SPP (the SPP presented in [22]). These layers of clusters show how the clusters can be arranged within layers, but there are variations (also regarding cluster composition), and Fig. 2 illustrates differences between individual layers of clusters rather than differences between 3C and 9C.

In the reconstructions, the detected amount of Ni was so low that it was not meaningful to include it in the cluster analysis of Fe–Cr clusters (presented in Section 4.3). However, Ni was detected in some grains and was by visual assessment observed to cluster in a few of them and was in one case by the use of radial distribution functions (RDFs) observed to co-cluster with Fe but not with Cr. In

Fig. 2. One layer of clusters from a 3C specimen (left) and one layer of clusters from a 9C specimen (right). Both layers are viewed approximately in the <*c*>-direction.

Table 2

Bulk (exclusive of SPPs) and matrix (exclusive also of clusters and grain boundaries) compositions (at.%) of 3C and 9C specimens. The ± indicates one sample standard deviation, between the evaluated specimens for the bulk composition and between the evaluated grains for the matrix composition.

	at.% Sn	at.% Fe	at.% Cr	at.% Ni
Bulk 3C	1.07±0.10	0.31±0.10	0.061±0.038	0.006±0.005
Bulk 9C	1.07±0.05	0.34±0.16	0.24±0.27	0.012±0.005
Matrix 3C	0.95±0.05	0.033±0.018	0.012±0.005	0.005±0.003
Matrix 9C	0.92±0.18	0.032±0.022	0.009±0.005	0.006±0.003

addition to the small amounts of Ni in some grains, at GBs, and at one <*c*>-component loop, there were also significant amounts detected in the remnants of two former SPPs, the observation of them published in [22] and [45].

4.2. Bulk composition and matrix chemistry

Table 2 shows the bulk composition (excluding SPPs) of the specimens that were evaluated in the analysis of Fe–Cr clusters and the matrix composition (excluding also GBs and Fe–Cr clusters) of the same specimens but excluding three small grains (one for 3C and two for 9C) due to the isosurfaces used not reliably separating the matrix from the clusters in these grains.

Regarding bulk composition, the concentrations of Sn and Fe after 3C are on average close to the total concentrations in the alloy, whereas the concentrations of Cr and Ni are on average lower than the alloy concentrations. After 9C, also the average Cr concentration is close to the alloy concentration. For Sn and Fe there is only a small difference between 3C and 9C, but for Cr and Ni the average concentration after 9C is higher by a factor of approximately 4 and 2, respectively. However, the large grain-to-grain variations and the few specimens evaluated might have influenced this result. The matrix composition is similar for 3C and 9C, with the Sn concentration being similar to the bulk concentration, the Fe concentration about one order of magnitude lower than the bulk concentration, the Cr concentration on average lower than the bulk concentration but with large variations, and the Ni concentration not very different from the bulk concentration. Fig. 3, which shows the concentration of Cr versus the concentration of Fe for individual grains (i.e. the concentration including Fe–Cr clusters but excluding GBs and SPPs), indicates that there might be a correlation between the concentrations of Fe and Cr.

4.3. Clustering of iron and chromium

Examples of one cluster each from the 3C specimens and the 9C specimens are shown in Fig. 4. These clusters reflect the aver-
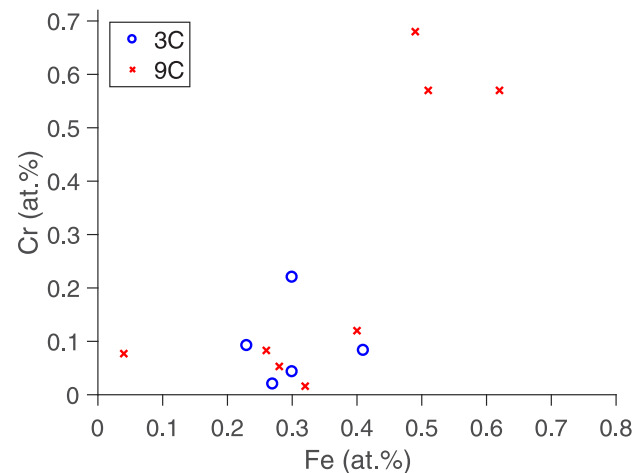

Fig. 3. Composition (including clusters and surrounding matrix but excluding GBs and SPPs) of Fe and Cr of the individual grains that were used for analysis of Fe–Cr clusters.

Table 3

Average results between individual grains in the cluster analysis. The ± indicates one sample standard deviation. (The detection efficiency of 0.37 of the APT instrument has been taken into account.)

	3C	9C
10^{23} clusters per m^3	4.4 ± 1.6	5.5 ± 3.4
Fe+Cr atoms per cluster	104±44	225±165
at.% Zr	75±3	77±4
at.% Sn	1.5 ± 0.2	1.8 ± 0.9
at.% Fe	16±5	12±7
at.% Cr	6.6 ± 5.5	9.2 ± 5.4

age differences between 3C and 9C, with the cluster after 9C being a little larger and more Cr rich. As there are large variations, there are clusters after both 3C and 9C that deviate from the composition and size depicted in Fig. 4. One of the large Cr-rich clusters with a non-spheroidal shape observed after 9C is shown in Fig. 5. Also among these large Cr-rich clusters, there are variations in composition and size, as well as in shape.

The average results of the cluster analysis are shown in Table 3, and Fig. 6 shows the results for the individual grains. The average values indicate that the cluster number density (number of clusters per m^3), the number of Fe and Cr atoms per cluster, and the Cr content of the clusters are higher after 9C than after 3C. However, the grain-to-grain variations are larger than the differences between 3C and 9C. In the clusters, the concentration of Fe is, on
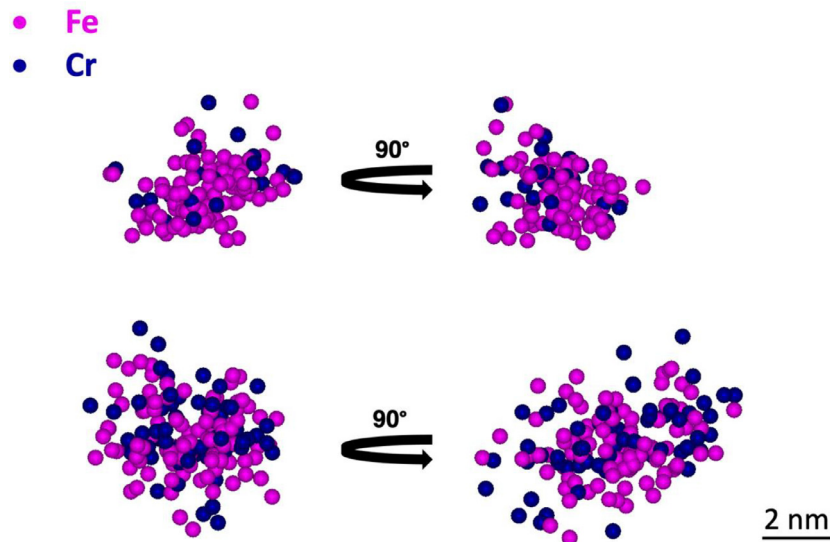
Fig. 4. One cluster from a 3C specimen (top) and one cluster from a 9C specimen (bottom) viewed in two directions perpendicular to each other.
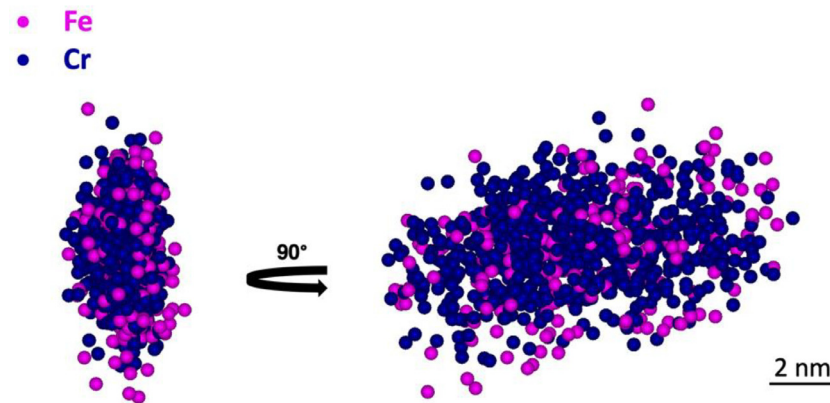

Fig. 5. One large Cr-rich cluster from a 9C specimen viewed in two directions perpendicular to each other.

average, higher than the concentration of Cr. There is also, on average, a small enrichment of Sn in the clusters.

The ratio Fe/(Fe+Cr) versus number of Fe and Cr atoms per cluster for the individual clusters is shown in Fig. 7. There is a higher number of large and Cr-rich clusters after 9C compared with 3C. This is consistent with the information given in Table 3 and Fig. 6. The majority of the large clusters are Cr rich. However, there is no clear correlation between Fe or Cr content and cluster size. The 22 largest clusters (all Cr rich) for 9C have been omitted to make it easier to compare at the same scale. Due to the higher number of evaluated 9C specimens, there is a higher total number of clusters for 9C in the diagram.

The cumulative relative cluster frequency after 3C and 9C is shown in Fig. 8. For 3C the median number of Fe and Cr atoms per cluster is 54, and the 90th percentile is 181. For 9C the median number of Fe and Cr atoms per cluster is 78, and the 90th percentile is 407.

4.4. <c>-component loops

Five ring-shaped features, having diameters in the approximate range 20–60 nm and interpreted to be <c>-component loops decorated with Sn, Fe, and Ni, were observed after 9C, three of these mainly decorated with Sn and two mainly decorated with Fe. Small amounts of Fe were observed at the <c>-component

loops mainly decorated with Sn, and small amounts of Sn and Ni (at one of the loops) were observed at the <c>-component loops mainly decorated with Fe. One of the <c>-component loops mainly decorated with Sn was located in one of the regions with Sn clusters described in Section 4.5. Figures showing some of the <c>-component loops can be found in [22]. After 3C, no <c>-component loops were observed.

4.5. Distribution of tin

Tin was observed to be anticorrelated with the layers of clusters of Fe and Cr in such a way that the concentration of Sn was higher between than inside these layers. This anticorrelation is similar to previous TEM and APT observations [21,26]. Fig. 9 shows a one-dimensional (1D) concentration profile (constructed using a cylindrical ROI of 80 nm diameter with a fixed bin width of 1 nm) across the layers of Fe–Cr clusters (i.e. the basal planes of the Zr matrix) in one grain of a 3C specimen (the lower grain in the reconstruction to the left in Fig. 1). The Fe and Cr concentrations rise when the Sn concentration drops and vice versa. Ni (not shown in Fig. 9) seems to follow the pattern of Fe and Cr approximately, but is not present in large enough amounts for a clear anticorrelation to be seen.

Clustering of Sn was observed in two grains or regions of grains that had very few clusters of Fe and Cr [22], and both of these
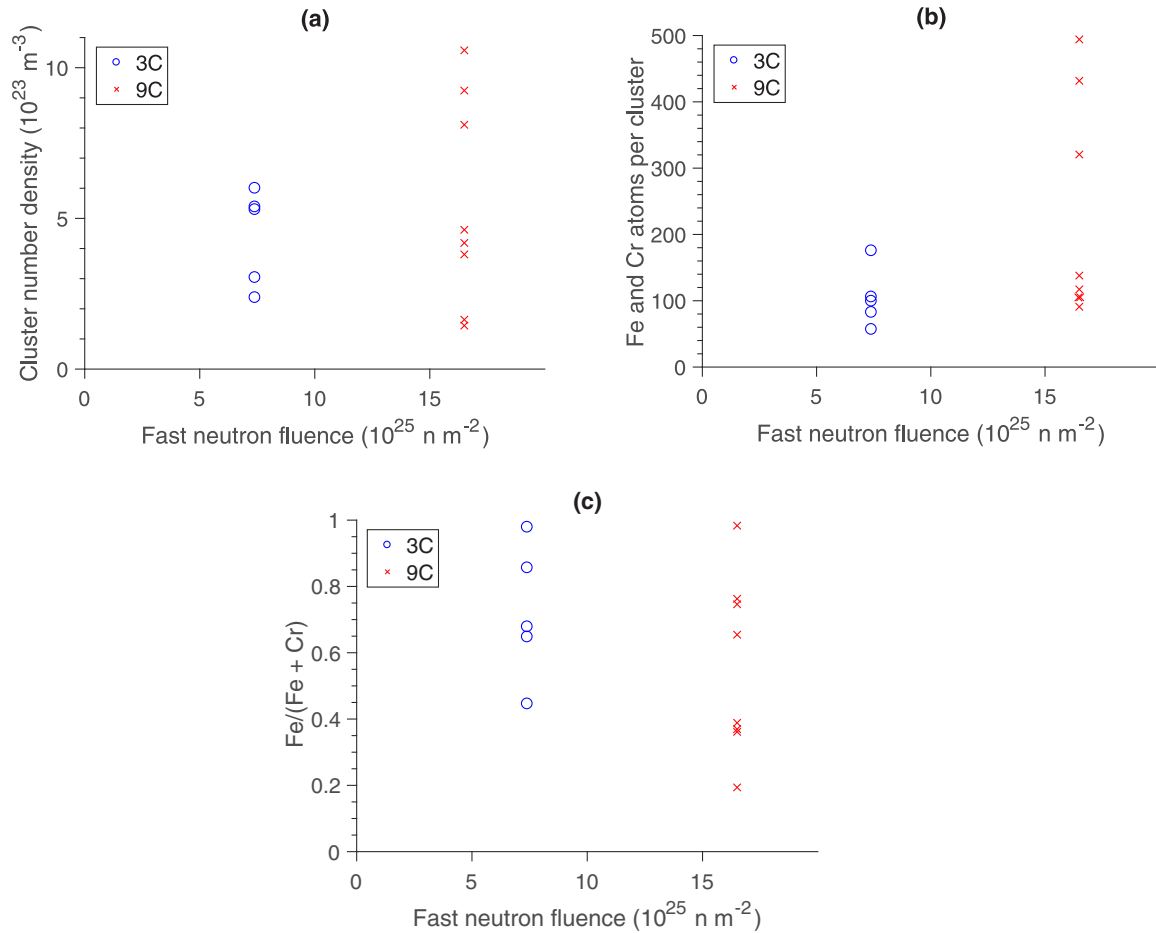
Fig. 6. (a) Cluster number density, (b) average number of Fe and Cr atoms per cluster, and (c) Fe/(Fe + Cr) in clusters for the evaluated grains (five for 3C and eight for 9C). (The detection efficiency of 0.37 of the APT instrument has been taken into account.)
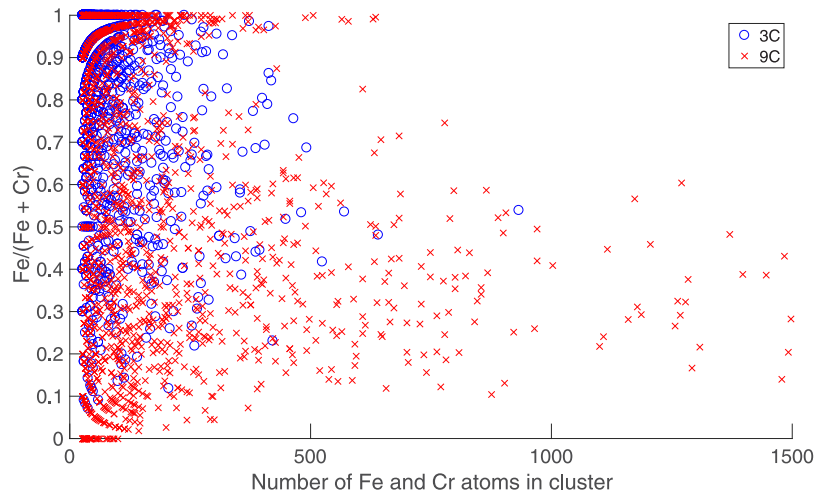

Fig. 7. Fe/(Fe+Cr) versus number of Fe and Cr atoms per cluster for the individual clusters. The 22 largest clusters (all Cr rich) after 9C have been omitted to enable a comparison at the same scale. (The detection efficiency of 0.37 of the APT instrument has been taken into account.)

grains or regions of grains were observed to be adjacent to a region that had higher O content and slightly lower H content and contained Fe and Cr. The Sn clusters were not observed to be aligned as the Fe–Cr clusters were. Both specimens containing regions with Sn clusters had been exposed for 9C. Cluster analysis using MSM yielded cluster number densities of 18×10^{23} and 14×10^{23} clusters/m³, which is higher than the values for Fe–Cr clusters, and an average number of Sn atoms per cluster of 57 and

64 in the two regions. No obvious clustering of Sn was observed in grains with many Fe–Cr clusters.

4.6. Grain boundaries

1D concentration profiles (constructed using a cylindrical ROI of 20 nm diameter with a fixed bin width of 1 nm) across a 3C GB and across a 9C GB (both believed to be sub-GBs) are shown in
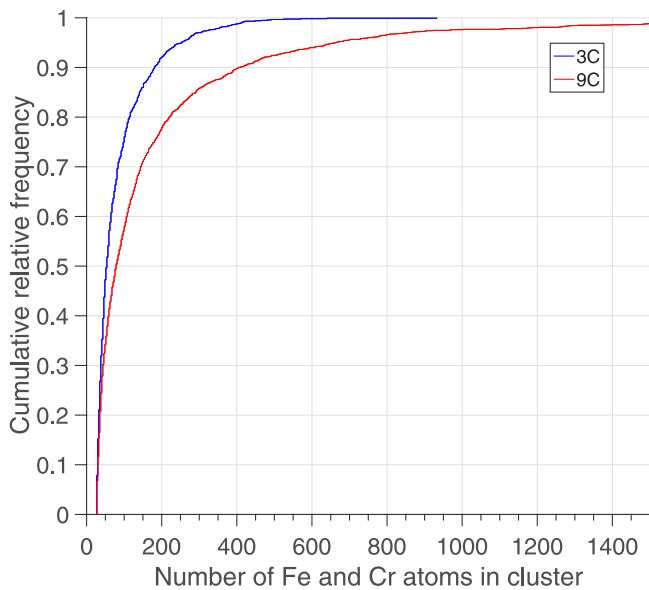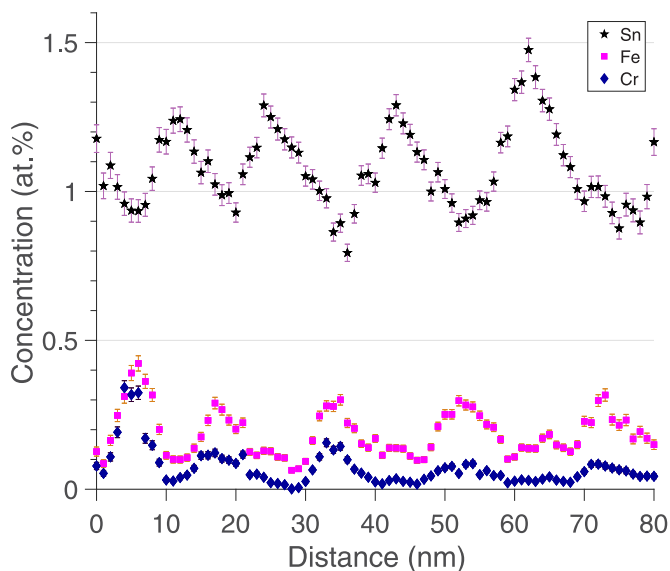
Fig. 8. Cumulative relative frequency of number of Fe and Cr atoms per cluster. The 22 largest clusters (all Cr rich) after 9C have been omitted to enable a comparison at the same scale. (The detection efficiency of 0.37 of the APT instrument has been taken into account.)

Fig. 9. 1D concentration profile across basal planes of the Zr matrix in one grain of a 3C specimen, showing that the Sn concentration is anticorrelated with the Fe and Cr concentrations. The error bars (smaller than the data markers where not visible) indicate one standard deviation of the counting statistics.

Fig. 10. At both GBs, there is enrichment of Sn and Fe, with the concentrations being around 2–3 at.%, and there is also a small enrichment of Cr and Ni. Taking the large variations in local chemistry into account, the interpretation of the measured values is that there are no large differences in chemistry at sub-GBs between 3C and 9C. Also the difference in concentrations of alloying elements between 3C and 9C seen some distance away from the GB is believed to be an effect of local chemistry variations and not to be due to the difference in exposure time. For both 3C and 9C the concentrations of Sn, Fe, and Ni are larger at the GB than in the surrounding matrix, including clusters in the ROI, but the concentration of Cr at the GB is not higher than in the clusters.

4.7. Analysis of an SPP

A partially dissolved $Zr(Fe,Cr)_2$ SPP was observed after 3C. Fig. 11 shows the distribution of Cr, Fe, Ni, and Si in the region containing the SPP, and a video of the rotating reconstruction is presented in Supplementary material. The layers of Fe–Cr clusters (sometimes called rafts) adjacent to the SPP are very similar to the layers of clusters close to SPPs observed with TEM in proton- and in neutron-irradiated Zircaloy-2 [10,21] and with TEM and APT in proton-irradiated Zircaloy-4 [64]. Fig. 12 shows the concentrations of Fe and Cr as a proxigram [65] and the average concentrations of H and Zr inside and outside the SPP computed using peak decomposition in IVAS (as these concentrations, in contrast to the concentrations of Fe and Cr, would be much affected by the incapacity to decompose peaks in the built-in proxigram function in IVAS). The Fe concentration is very low and almost constant inside the part of the SPP covered by the APT analysis, with an Fe/Cr ratio below 1/10. The H concentration was measured to be 14 at.% outside and 6 at.% inside the SPP. Difficulties associated with analysing H with APT [61,62] should be kept in mind when interpreting this result.

To estimate the possible influence of a difference in evaporation field between the SPP and the matrix, the ratio Zr^{3+}/Zr^{2+} (including ZrH species) was calculated. This ratio was 0.06 inside and 0.02 outside the SPP, indicating that the evaporation field was only slightly higher for the SPP [56]. Since H adsorption from the residual H_2 in the vacuum chamber might be field dependant [61], the small field difference observed suggests that the large difference in H concentration measured reflects a real composition difference between the phases rather than a difference in H adsorption onto the two phases.

5. Discussion

5.1. Matrix chemistry and clustering of iron and chromium

The large variations in chemistry between, and sometimes within, grains after 3C are not surprising, as a similar observation after 9C was made in the previous study by Sundell et al. [22]. Also the study by Sawabe and Sonoda indicated that there are grain-to-grain variations and that the distance to partially dissolved SPPs affects the local chemistry, including that of clusters [23]. As almost all our analyses indicated low Ni content, it seems that the specimen volumes studied in this work were closer to dissolved or partially dissolved $Zr(Fe,Cr)_2$ SPPs than $Zr_2(Fe,Ni)$ SPPs.

The observation of a higher concentration of Cr both in the clusters and in the bulk (excluding SPPs) and of Ni in the bulk (excluding SPPs) after 9C compared with 3C, albeit with large grain-to-grain variations, should be expected, since $Zr(Fe,Cr)_2$ SPPs are on average smaller and have a higher number density [9,10,66–68] and have been observed to start to dissolve earlier [9,10,13] than $Zr_2(Fe,Ni)$ SPPs. In the as-produced material almost all Cr is found in $Zr(Fe,Cr)_2$ SPPs and almost all Ni in $Zr_2(Fe,Ni)$ SPPs, and after 9C not fully dissolved SPPs of both types have been observed [10,13], although complete dissolution of small SPPs, which predominantly are of $Zr(Fe,Cr)_2$ type, has been reported [13]. A combination of the behaviour of the SPPs under irradiation and the higher total Cr than Ni content of the material should make it more likely to encounter a region rich in Cr than a region rich in Ni in the small volume covered by an APT analysis. This is in line with the cluster content being Fe and Cr as observed in this work (and in the work by Sundell et al. [22]) and in the work by Sawabe and Sonoda [23]. In none of these studies, clusters containing substantial amounts of Ni were observed. Ni-rich APT specimens not containing SPPs have been reported in only a few cases [25].
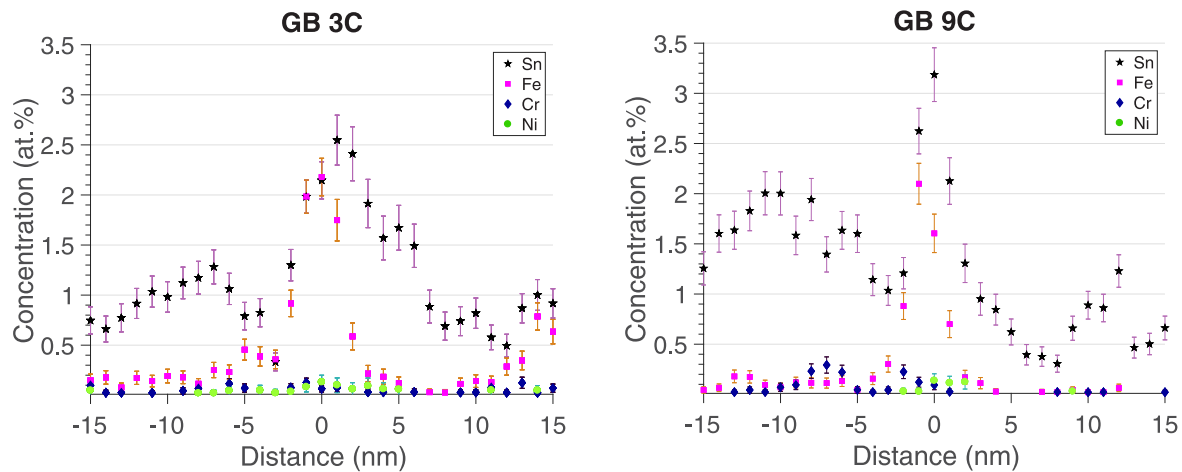
Fig. 10. 1D concentration profiles across a 3C GB and a 9C GB (with the GBs centred at approximately 0 nm). Concentrations that are equal to zero are not displayed. The error bars (smaller than the data markers where not visible) indicate one standard deviation of the counting statistics.
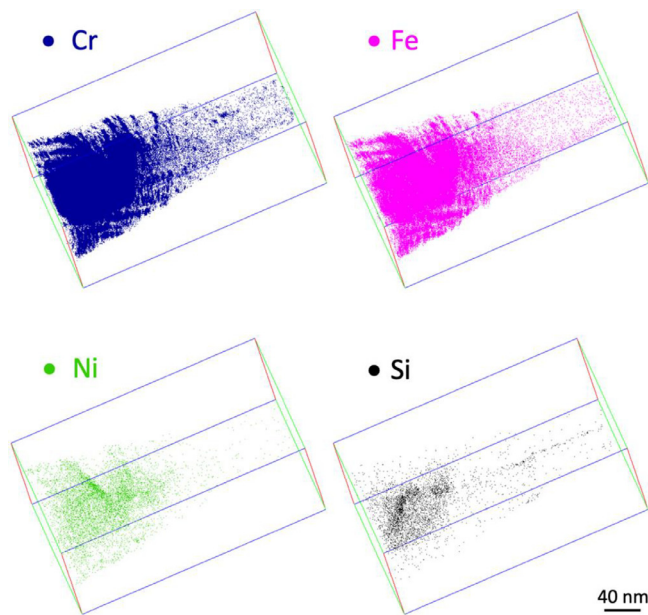

Fig. 11. Distribution of Cr, Fe, Ni, and Si in a 3C specimen containing the remnants of a partially dissolved $Zr(Fe,Cr)_2$ SPP. The size of the box is $152 \times 148 \times 289$ nm^3 (red × green × blue). (For interpretation of the references to colour in this figure legend, the reader is referred to the web version of this article.)

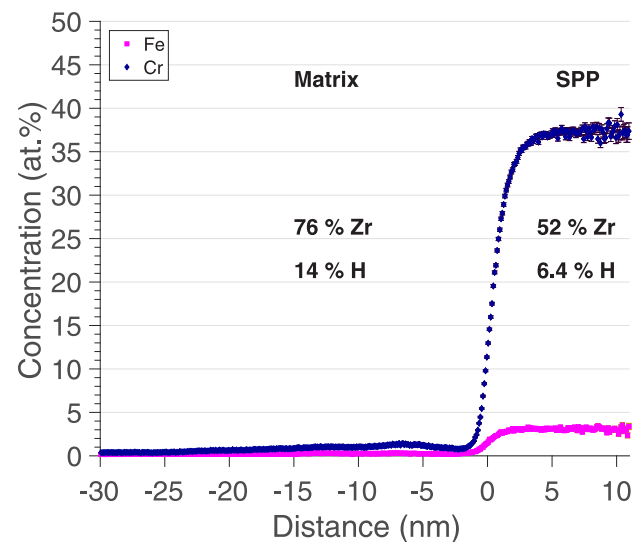**Fig. 12.** Proxigram from the surface of a partially dissolved $Zr(Fe,Cr)_2$ SPP (the SPP in Fig. 11). The measured hydrogen concentration is higher outside than inside the SPP. The error bars (smaller than the data markers where not visible) indicate one standard deviation of the counting statistics.

In comparison with the Fe–Ni-rich region reported in [25], the matrix (excluding SPPs, GBs, and clusters) of the Fe–Cr-rich regions in this work, on average, has a slightly lower Fe concentration, a higher Cr concentration, and a much lower Ni concentration. However, the large grain-to-grain variations and the few observations of Fe–Ni-rich regions should be kept in mind when interpreting this result. Our measured concentration of Fe in the matrix, using isosurfaces, is on average lower than that reported by Sawabe and Sonoda using MSM [23]. As the materials in the two studies were very similar, it is not unlikely that the difference in methodology is the reason for the difference in results. Furthermore, there seems to be no change in matrix composition with fluence in either of the two studies. In comparison with the matrix concentration of Fe measured with APT in an Nb-containing Zr alloy after exposure to 16.5×10^{25} n m^{-2} ($E > 1$ MeV) [69], our measured concentration after both 3C and 9C is on average a little lower but not very different.

In this and previous studies using APT in laser mode [22,23], the shape of the Fe–Cr clusters observed does not reveal any information about the association to <a>-loops and does not agree with what has been predicted in MD and MC simulations for accumulation of Fe [30] and Ni [29] at <a>-loops. However, the results of those simulations agree with the observations of Fe–Ni clusters using voltage-pulsed APT, which has a somewhat higher spatial resolution than laser-pulsed APT (especially for instruments having a green laser [70]) and therefore usually a better capability of cluster detection [71]. With voltage-pulsed APT Fe–Cr clusters appeared spheroidal at expected positions of <a>-loops, but Fe–Ni clusters appeared disc-shaped (also at expected positions of <a>-loops) [25]. As the Fe–Cr clusters appear spheroidal, it is unclear exactly how the clusters are related to the <a>-loops. They can be located inside the loops, or they can be located next to the loops.

The results obtained from the cluster analysis are not straightforward to interpret in terms of differences between 3C and 9C, as the grain-to-grain variations of both exposure times, especially 9C, are large. Sawabe and Sonoda observed that the cluster number density reached a constant value at a fluence close to that of

our 3C specimens, indicating that the number of $<a>$-loops had reached a value that remained constant with respect to fluence [23]. However, from the TEM study by Harte et al. [21] and an X-ray line profile analysis (XLPA) study by Ungár et al. [51] it seems that there might be a slight increase in $<a>$-loop number density from 3C to 9C. Our results do not give a clear indication of whether or not the $<a>$-loop number density continues to increase slightly with increasing fluence after 3C.

In both the study by Harte et al. [21] and a study by Carpenter and Northwood [20], the $<a>$-loop number density at the fluences closest to those in our study is reported to be in the approximate range 1–3×10^{22} m^{-3} from TEM measurements. This number density is clearly lower than our observed cluster number density of 1–11×10^{23} m^{-3}. However, the cluster number density observed by Sawabe and Sonoda [23], using APT, at neutron fluences similar to those of our samples is in better agreement with our observed cluster number density (although they reported a slightly lower average value of approximately 3×10^{23} m^{-3}). The difference between the reported $<a>$-loop number density in the TEM studies [20,21] and our observed cluster number density (and also that by Sawabe and Sonoda [23]) could be due either to that several clusters can be associated with one loop or to that some loops were missed in the TEM studies. The XLPA study by Ungár et al. indicates that the smallest $<a>$-loops are often not recognised in TEM studies [51].

The, on average, larger number of atoms per cluster after 9C is most probably an effect of more Fe and Cr atoms being available after dissolution from SPPs. From the study by Harte et al., it appears that the loop size (diameter) does not increase with increasing fluence [21] and therefore should not be a factor influencing the number of atoms per cluster. The fact that Cr-rich clusters often are large might be due to the fact that Cr is dissolved from SPPs later than Fe and joins existing Fe-rich clusters that thereby become larger and Cr rich. However, there might also be other mechanisms leading to larger Cr-rich clusters (preferentially located close to GBs). Such mechanisms could involve differences in (bulk and GB) diffusivity [72] and solubility between Fe and Cr. Sawabe and Sonoda attributed their observation of an increase in cluster size with increasing fluence to the number of cluster sites being limited to a saturated number of $<a>$-loops [23].

5.2. $<c>$-component loops

The segregation of Sn to ring-shaped features (the presumed $<c>$-component loops) observed in this study (and in the study by Sundell et al. [22]) is in accordance with the prediction of segregation of Sn to basal stacking faults in density functional theory (DFT) modelling by March-Rico et al. [73]. Also their prediction of segregation of Fe to basal stacking faults agrees well with our observation of Fe together with Sn at the ring-shaped features. However, our observation of Ni at one of the presumed $<c>$-component loops does not agree with their predicted absence of Ni at basal stacking faults. As mentioned in the study by Sundell et al. [22], our observed presumed $<c>$-component loops were small compared with $<c>$-component loops observed with TEM [14,21]. Due to the small volume of an APT analysis, however, only small $<c>$-component loops can be detected in their full size. That no $<c>$-component loops were observed after 3C is not surprising, as, if there are $<c>$-component loops already after 3C, their number density should be much lower than after 9C [14,21].

5.3. Clustering of tin

Our observation of the Sn clusters not being aligned and their number density being higher than that of Fe–Cr clusters might indicate that Sn clusters are not related to $<a>$-loops in the same

way Fe–Cr clusters are. The fact that Sn clusters were observed in grains or parts of grains that were adjacent to grains with a higher O content, after 9C but not after 3C, gives an indication that there could be a relation between Sn-clustering and hydride phases. Although only a slightly enhanced H concentration was observed in the regions with Sn clusters compared with the adjacent regions without Sn clusters, it is still possible that these regions were hydride phases during reactor operation and that the adjacent regions were not. The reason for not observing more H in these regions might be related to difficulties in measuring H with APT or redistribution of H after reactor operation (see Section 5.5 for more discussion on H).

Our hypothesis that the regions with Sn clusters were hydrides that were depleted in Fe and Cr is in line with the electron probe microanalysis (EPMA) and TEM observations by Baris et al., where the content of alloying elements was lower in hydride phases compared with the matrix [46,47]. The formation of clusters is in line with the results of an APT study on unirradiated deuterium-charged Zircaloy-4 by Breen et al., where the Sn solubility was lower in deuteride phases compared with the Zr matrix (although no Sn clusters were observed) [74]. Modelling by Christensen et al. predicts that Sn, Fe, Cr, and Ni prefer α-Zr over hydride phases, with this preference being most pronounced for Sn [75]. It is thus possible that the Sn clusters observed in our analyses were formed when Sn was incorporated into a hydride phase. The very low number of clusters of Fe, Cr, and Ni in these regions might possibly be explained by the faster diffusion of these elements compared with Sn [72], so that they were able to migrate to the Zr matrix upon formation of the hydride. If the Sn clusters are related to $<a>$-loops in the same way Fe–Cr clusters are, our results might be an indication that the $<a>$-loop number density is higher in hydride phases than in α-Zr.

5.4. Grain boundary segregation

The enrichment of Sn and Fe at GBs observed in this study agrees with previous APT observations [22,23]. The observation of enrichment of small amounts of Cr at GBs made in this study was not recognised in the study by Sundell et al. [22] but is in agreement with the observations made by Sawabe and Sonoda [23]. Also our observation of Cr-rich clusters often being located close to GBs is in line with the results of Sawabe and Sonoda [23]. Observation of enrichment of Ni at GBs, as made in this study (although of low concentration with relatively large standard deviation), was not made in the previous APT studies [22,23]. Our results for Ni indicate that Ni can be found at GBs or sub-GBs when available after dissolution from SPPs or that it can be found at sub-GBs after depletion from GBs of the original microstructure. Enrichment of Fe and Ni, but not Cr, has been observed with APT at GBs or sub-GBs in autoclave-tested Zircaloy-2 [76] and with TEM both in as-produced and in-reactor-exposed Zircaloy-2 [47]. Enrichment of Sn has also been observed with TEM after in-reactor exposure [47]. The enrichment of Sn, Fe, Cr, and Ni at GBs due to a thermodynamic driving force has been predicted by Christensen et al. [75].

5.5. SPPs and hydrogen

The much higher concentration of Cr compared with Fe inside the SPP shown in Fig. 11 indicates that Fe has been preferentially dissolved from the SPP, as the Fe/Cr ratio of $Zr(Fe,Cr)_2$ SPPs in the as-produced material is expected to be much higher than our measured value below 1/10 [9,10,13,68]. The lower concentration of Fe compared with Cr outside the SPP is likely due to its earlier expulsion [9–11,13] and its higher diffusivity [72]. The observation of Ni and Si in $Zr(Fe,Cr)_2$ SPPs is not surprising, since Ni and Si previously have been observed in $Zr(Fe,Cr)_2$ SPPs [10,77].

In both the SPP shown in Fig. 11 and the SPP investigated by Sundell et al. [22], all of the elements Fe, Cr, Ni, and Si can be seen. In one of the TEM studies by Harte et al., Ni was observed in $Zr(Fe,Cr)_2$ SPPs, but Cr was not observed in $Zr_2(Fe,Ni)$ SPPs [10]. In an APT study by Sawabe et al., relatively large amounts of Ni and Si were observed in $Zr(Fe,Cr)_2$ SPPs, but only very small amounts of Cr were observed in $Zr_2(Fe,Ni)$ SPPs [77]. It is thus not unlikely that the SPP in the study by Sundell et al. [22] was a $Zr(Fe,Cr)_2$ SPP rather than a $Zr_2(Fe,Ni)$ SPP.

As the measured H concentration of the 3C specimens was similar to that of the 9C specimens [22,25], they might have been hydride phases during analysis. It is also possible that the hydrogen content was in part due to the residual gas in the analysis chamber of the APT instrument [61,62]. As the rod average hydrogen content of the 3C sample of 0.4 at.% is below the solubility limit at reactor operating temperatures [32], the possible hydride phases were most likely not present during reactor operation. The observations for the 3C specimens can thus be assumed to be representative of the metal during operation. To encounter hydrides that were not present during reactor operation in the analyses should not be surprising, as hydrides in the cladding are known to reorient post service, due to temperature changes, and reprecipitate in the metal close to the outer surface [78] (the region studied in this work). Also during yearly outages and other shutdowns of the reactor, hydrogen and hydrides are redistributed [78]. Furthermore, hydrogen redistribution and hydride formation can occur during sample and specimen preparation, e.g. in the FIB [59,60]. In contrast to the rather low hydrogen content of the rod of the 3C sample, the hydrogen content of 6 at.% of the rod of the 9C sample is above the solubility limit at operating conditions [32]. There might thus be regions in the 9C specimens that were hydride phases during reactor operation (e.g. the observed regions with Sn clusters). However, as there are large similarities between most of the 3C and the 9C specimens (most notably the existence of Fe–Cr clusters aligned in layers normal to the $<c>$-direction), most of the observations after 9C can be assumed to be representative of the metal during reactor operation.

Although the measured higher H concentration outside than inside the partially dissolved $Zr(Fe,Cr)_2$ SPP might not be representative of the H distribution during operation, it agrees with the results of previous measurements using various techniques and should therefore be of interest to report, at least from an analysis perspective. Lower H content inside a $Zr(Fe,Cr)_2$ SPP compared with the surrounding matrix in unirradiated Zircaloy-4 has been measured with APT [79]. Deuterium has with nanoscale secondary ion mass spectrometry (nanoSIMS) been observed to be preferentially located in the Zr matrix surrounding $Zr(Fe,Cr)_2$ SPPs in Zircaloy-2 and Zircaloy-4 corroded in deuterated water [80]. TEM observations have been made of hydrides being present in the Zr matrix, but not in the SPP, at the matrix/SPP interface in hydrogen-charged unirradiated Zircaloy-4 [81]. In the oxide of Zircaloy-4 corroded in deuterated water, deuterium hotspots have with nanoSIMS been observed not to be correlated with $Zr(Fe,Cr)_2$ SPPs [82]. There is also DFT modelling that suggests that $Zr(Fe,Cr)_2$ SPPs (as opposed to $Zr_2(Fe,Ni)$ SPPs) do not offer preferential sites for H accommodation [80,83].

5.6. Relation between microstructure and breakaway

The difference between 3C and 9C regarding clustering is relatively small. The cluster number density is similar, and it seems unlikely that the increase in cluster size should be decisive for breakaway in corrosion, in HPU, or in growth to occur. On the other hand, one could envisage that the removal of a large amount of the $Zr(Fe,Cr)_2$ SPPs or the increased release of Ni from $Zr_2(Fe,Ni)$ SPPs after 9C is important for breakaway. Ni has been observed to in-

crease HPU [35,84,85], and the increase of Ni outside SPPs might thus be one of the causes for breakaway in HPU. The increase of Fe and Ni outside SPPs might be of importance for the formation and/or stabilisation of $<c>$-component loops, which in turn may be important for accelerated corrosion or growth. It is obviously difficult to determine the root cause of breakaway, but the present study has contributed with some important observations by comparing the microstructure before (3C) and after (9C) breakaway.

6. Conclusions

In this study of the metal close to the metal/oxide interface in Zircaloy-2 exposed to three and nine annual cycles of operation in a commercial BWR, corresponding to before and after the onset of acceleration in corrosion, hydrogen pickup, and growth, the following observations have been made:

- Overall, large variations in local chemistry between individual specimens and individual grains were observed. There was on average more Cr and Ni in the bulk (i.e. the total composition of matrix, clusters, and boundaries but excluding SPPs) after nine cycles than after three, but the grain-to-grain variations were larger than the difference between three and nine cycles.
- Clusters of Fe and Cr were located in layers typical of layers of aligned $<a>$-loops. The cluster number density was on average slightly higher and the clusters were on average larger and richer in Cr after nine cycles than after three cycles, but the grain-to-grain variations were larger than the differences between the two exposure times. Large Cr-rich clusters were generally located close to GBs or sub-GBs. Ni was observed in clusters in only a few grains. Sn was on average slightly enriched in the Fe–Cr clusters, but the concentration of Sn was higher between than inside the layers of Fe–Cr clusters. Clusters of Sn were observed in regions that were depleted of Fe and Cr and that were located adjacent to regions with higher O content.
- Features that appeared to be $<c>$-component loops were observed after nine cycles but not after three cycles. Enrichment of Sn and Fe was observed at all of the $<c>$-component loops, with one of these elements in much higher concentration than the other at each individual loop. Ni was seen to be enriched at one loop where there was more enrichment of Fe than Sn.
- Enrichment of Sn, Fe, and small amounts of Cr and Ni at GBs or sub-GBs was observed. There seems to be no general difference between three and nine cycles regarding the concentrations of these elements at GBs.
- A partially dissolved $Zr(Fe,Cr)_2$ SPP that was observed after three cycles had an Fe/Cr ratio lower than 1/10 and also contained Ni and Si.

Declaration of Competing Interest

The authors declare that they have no known competing financial interests or personal relationships that could have appeared to influence the work reported in this paper.

CRediT authorship contribution statement

Acknowledgements

Supplementary materials

Supplementary material associated with this article can be found, in the online version, at doi:10.1016/j.jnucmat.2022.153537.

References

[1] B. Wadman, H.-O. Andrén, Microanalysis of the matrix and the oxide-metal interface of uniformly corroded Zircaloy, ASTM STP 1132 (1991) 461–475, doi:10.1520/stp25522s.

[2] R.M. Kruger, R.B. Adamson, S.S. Brenner, Effects of microchemistry and precipitate size on nodular corrosion resistance of Zircaloy-2, J. Nucl. Mater. 189 (1992) 193–200, doi:10.1016/0022-3115(92)90532-P.

[3] A. Yilmazbayhan, O. Delaire, A.T. Motta, R.C. Birtcher, J.M. Maser, B. Lai, Determination of the alloying content in the matrix of Zr alloys using synchrotron radiation microprobe X-ray fluorescence, J. Nucl. Mater. 321 (2003) 221–232, doi:10.1016/S0022-3115(03)00267-8.

[4] B. Hutchinson, B. Lehtinen, M. Limbäck, M. Dahlbäck, A study of the structure and chemistry in Zircaloy-2 and the resulting oxide after high temperature corrosion, ASTM STP 1505 (2009) 269–284, doi:10.1520/JAI101106.

[5] M. Ivermark, Characterisation of the Matrix Chemistry in Zirconium Alloys, University of Manchester, 2009 Ph.D. thesis.

[6] G. Sundell, Atomic Scale Degradation of Zirconium Alloys For Nuclear Applications, Chalmers University of Technology, 2015 Ph.D. thesis.

[7] C. Lemaignan, A.T. Motta, Zirconium alloys in nuclear applications, in: R.W. Cahn, P. Haasen, E.J. Kramer (Eds.), Materials science and technology – a comprehensive treatment, Volume 10B: Nuclear Materials Part II (Chapter 7), Volume Editor B.T. Frost, 1994, doi:10.1002/adma.19950071220.

[8] P. Chemelle, D.B. Knorr, J.B. van der Sande, R.M. Pelloux, Morphology and composition of second phase particles in Zircaloy-2, J. Nucl. Mater. 113 (1983) 58–64, doi:10.1016/0022-3115(83)90166-6.

[9] S. Abolhassani, D. Gavillet, F. Groeschel, P. Jourdain, H.U. Zwicky, Recent observations on the evolution of the secondary phase particles in Zircaloy-2 under Irradiation in a BWR up to a high burnup, in: Proceedings of International Topical Meeting on LWR Fuel Performance, April 10–13, Park City, Utah, USA, 2000, pp. 470–484.

[10] A. Harte, M. Topping, P. Frankel, D. Jädernäs, J. Romero, L. Hallstadius, E.C. Darby, M. Preuss, Nano-scale chemical evolution in a proton-and neutron-irradiated Zr alloy, J. Nucl. Mater. 487 (2017) 30–42, doi:10.1016/j.jnucmat.2017.01.049.

[11] Y. Etoh, S. Shimada, Neutron irradiation effects on intermetallic precipitates in Zircaloy as a function of fluence, J. Nucl. Mater. 200 (1993) 59–69, doi:10.1016/0022-3115(93)90009-N.

[12] M. Griffiths, R.W. Gilbert, G.J.C. Carpenter, Phase instability, decomposition and redistribution of intermetallic precipitates in Zircaloy-2 and -4 during neutron irradiation, J. Nucl. Mater. 150 (1987) 53–66, doi:10.1016/0022-3115(87)90093-6.

[13] S. Valizadeh, G. Ledergerber, S. Abolhassani, D. Jädernäs, M. Dahlbäck, E.V. Mader, G. Zhou, J. Wright, L. Hallstadius, Effects of secondary phase particle dissolution on the in-reactor performance of BWR cladding, ASTM STP 1529 (2011) 729–753, doi:10.1520/JAI103025.

[14] M. Griffiths, A review of microstructure evolution in zirconium alloys during irradiation, J. Nucl. Mater. 159 (1988) 190–218, doi:10.1016/0022-3115(88)90093-1.

[15] P.M. Kelly, R.G. Blake, The characterization of dislocation loops in neutron irradiated zirconium, Philos. Mag. 28 (1973) 415–426, doi:10.1080/14786437308217463.

[16] A. Jostsons, P.M. Kelly, R.G. Blake, The nature of dislocation loops in neutron irradiated zirconium, J. Nucl. Mater. 66 (1977) 236–256, doi:10.1016/0022-3115(77)90113-1.

[17] A. Jostsons, R.G. Blake, J.G. Napier, P.M. Kelly, K. Farrell, Faulted loops in neutron-irradiated zirconium, J. Nucl. Mater. 68 (1977) 267–276, doi:10.1016/0022-3115(77)90251-3.

[18] A. Jostsons, P.M. Kelly, R.G. Blake, K. Farrell, Neutron irradiation-induced defect structures in zirconium, ASTM STP 683 (1979) 46–61, doi:10.1520/STP38157S.

[19] M. Griffiths, R.W. Gilbert, The formation of c-component defects in zirconium alloys during neutron irradiation, J. Nucl. Mater. 150 (1987) 169–181, doi:10.1016/0022-3115(87)90072-9.

[20] G.J.C. Carpenter, D.O. Northwood, The contribution of dislocation loops to radiation growth and creep of Zircaloy-2, J. Nucl. Mater. 56 (1975) 260–266, doi:10.1016/0022-3115(75)90041-0.

[21] A. Harte, D. Jädernäs, M. Topping, P. Frankel, C.P. Race, J. Romero, L. Hallstadius, E.C. Darby, M. Preuss, The effect of matrix chemistry on dislocation evolution in an irradiated Zr alloy, Acta Mater. 130 (2017) 69–82, doi:10.1016/j.actamat.2017.03.024.

[22] G. Sundell, M. Thuvander, P. Tejland, M. Dahlbäck, L. Hallstadius, H.-O. Andrén, Redistribution of alloying elements in Zircaloy-2 after in-reactor exposure, J. Nucl. Mater. 454 (2014) 178–185, doi:10.1016/j.jnucmat.2014.07.072.

[23] T. Sawabe, T. Sonoda, Evolution of nanoscopic iron clusters in irradiated zirconium alloys with different iron contents, J. Nucl. Sci. Technol. 55 (2018) 1110–1118, doi:10.1080/00223131.2018.1479987.

[24] B.V. Cockeram, P.D. Edmondson, K.J. Leonard, B.F. Kammenzind, J.L. Hollenbeck, Atom probe examinations of Zircaloy irradiated at nominally 358°C, Nucl. Mater. Energy. 19 (2019) 416–432, doi:10.1016/j.nme.2019.03.023.

[25] J. Eriksson, G. Sundell, P. Tejland, H.-O. Andrén, M. Thuvander, An atom probe tomography study of the chemistry of radiation-induced dislocation loops in Zircaloy-2 exposed to boiling water reactor operation, J. Nucl. Mater. 550 (2021) 152923, doi:10.1016/j.jnucmat.2021.152923.

[26] B.M. Jenkins, J. Haley, M.P. Moody, J.M. Hyde, C.R.M. Grovenor, APT and TEM study of behaviour of alloying elements in neutron-irradiated zirconium-based alloys, Scr. Mater. 208 (2022) 114323, doi:10.1016/j.scriptamat.2021.114323.

[27] D.O. Northwood, R.W. Gilbert, L.E. Bahen, P.M. Kelly, R.G. Blake, A. Jostsons, P.K. Madden, D. Faulkner, W. Bell, R.B. Adamson, Characterization of neutron irradiation damage in zirconium alloys — an international "round-robin" experiment, J. Nucl. Mater. 79 (1979) 379–394, doi:10.1016/0022-3115(79)90103-X.

[28] C. Dai, L. Balogh, Z. Yao, M.R. Daymond, The habit plane of ⟨a⟩-type dislocation loops in α-zirconium: an atomistic study, Philos. Mag. 97 (2017) 944–956, doi:10.1080/14786435.2017.1287441.

[29] C. Dai, P. Saidi, Z. Yao, M.R. Daymond, Atomistic simulations of Ni segregation to irradiation induced dislocation loops in Zr-Ni alloys, Acta Mater. 140 (2017) 56–66, doi:10.1016/j.actamat.2017.08.016.

[30] C. Dai, F. Long, P. Saidi, L.K. Béland, Z. Yao, M.R. Daymond, Primary damage production in the presence of extended defects and growth of vacancy-type dislocation loops in hcp zirconium, Phys. Rev. Mater. 3 (2019) 043602, doi:10.1103/PhysRevMaterials.3.043602.

[31] B. Cox, Some thoughts on the mechanisms of in-reactor corrosion of zirconium alloys, J. Nucl. Mater. 336 (2005) 331–368, doi:10.1016/j.jnucmat.2004.09.029.

[32] J. Bair, M. Asle Zaeem, M. Tonks, A review on hydride precipitation in zirconium alloys, J. Nucl. Mater. 466 (2015) 12–20, doi:10.1016/j.jnucmat.2015.07.014.

[33] R.B. Adamson, C.E. Coleman, M. Griffiths, Irradiation creep and growth of zirconium alloys: a critical review, J. Nucl. Mater. 521 (2019) 167–244, doi:10.1016/j.jnucmat.2019.04.021.

[34] B. Cheng, R. Adamson, Mechanistic studies of Zircaloy nodular corrosion, ASTM STP 939 (1987) 387–416, doi:10.1520/stp28134s.

[35] W.E. Berry, D.A. Vaughan, E.L. White, Hydrogen pickup during aqueous corrosion of zirconium alloys, Corrosion. 17 (1961) 109t–117t, doi:10.5006/0010-9312-17.3.81.

[36] G. Ledergerber, S. Abolhassani, M. Limbäck, R.J. Lundmark, K.-Å. Magnusson, Characterization of high burnup fuel for safety related fuel testing, J. Nucl. Sci. Technol. 43 (2006) 1006–1014, doi:10.1080/18811248.2006.9711189.

[37] G. Kuri, C. Degueldre, J. Bertsch, S. Abolhassani, Micro-focussed XAFS spectroscopy to study Ni-bearing precipitates in the metal of corroded Zircaloy-2, Appl. Phys. A Mater. Sci. Process. 98 (2010) 625–633, doi:10.1007/s00339-009-5456-z.

[38] G. Ledergerber, S. Valizadeh, J. Wright, M. Limbäck, L. Hallstadius, D. Gavillet, S. Abolhassani, F. Nagase, T. Sugiyama, W. Wiesenack, T. Tverberg, Fuel performance beyond design – exploring the limits, in: LWR Fuel Perform. Meet./Top Fuel/WRFPM, Orlando, Florida, USA, 2010, pp. 513–524.

[39] S. Abolhassani, G. Bart, J. Bertsch, M. Grosse, L. Hallstadius, A. Hermann, G. Kuri, G. Ledergerber, C. Lemaignan, M. Martin, S. Portier, C. Proff, R. Restani, S. Valance, S. Valizadeh, H. Wiese, Corrosion and hydrogen uptake in zirconium claddings irradiated in light water reactors, ASTM STP 1543 (2015) 540–573, doi:10.1520/STP154320130007.

[40] A. Harte, T. Seymour, E.M. Francis, P. Frankel, S.P. Thompson, D. Jädernäs, J. Romero, L. Hallstadius, M. Preuss, Advances in synchrotron x-ray diffraction and transmission electron microscopy techniques for the investigation of microstructure evolution in proton- and neutron-irradiated zirconium alloys, J. Mater. Res. 30 (2015) 1349–1365, doi:10.1557/jmr.2015.65.

[41] T. Seymour, P. Frankel, L. Balogh, T. Ungár, S.P. Thompson, D. Jädernäs, J. Romero, L. Hallstadius, M.R. Daymond, G. Ribárik, M. Preuss, Evolution of dislocation structure in neutron irradiated Zircaloy-2 studied by synchrotron x-ray diffraction peak profile analysis, Acta Mater. 126 (2017) 102–113, doi:10.1016/j.actamat.2016.12.031.

[42] M. Chollet, S. Valance, S. Abolhassani, G. Stein, D. Grolimund, M. Martin, J. Bertsch, Synchrotron X-ray diffraction investigations on strains in the oxide layer of an irradiated Zircaloy fuel cladding, J. Nucl. Mater. 488 (2017) 181–190, doi:10.1016/j.jnucmat.2017.03.010.

[43] A. Baris, S. Abolhassani, Y.L. Chiu, H.E. Evans, Observation of crack microstructure in oxides and its correlation to oxidation and hydrogen-uptake by 3D FIB Tomography — case of Zr-ZrO$_2$ in reactor, Mater. High Temp. 35 (2018) 14–21, doi:10.1080/09603409.2017.1392412.

[44] A. Garner, F. Baxter, P. Frankel, M. Topping, A. Harte, T. Slater, P. Tejland, J.E. Romero, E.C. Darby, A. Cole-Baker, M. Gass, M. Preuss, Investigating the effect of zirconium oxide microstructure on corrosion performance: a comparison between neutron, proton, and nonirradiated oxides, ASTM STP 1597 (2018) 491–523, doi:10.1520/stp159720160069.

[45] M. Topping, A. Harte, P. Frankel, C. Race, G. Sundell, M. Thuvander, H.-O. Andrén, D. Jädernäs, P. Tejland, J.E. Romero, E.C. Darby, S. Dumbill, L. Hallstadius, M. Preuss, The effect of iron on dislocation evolution in model and

commercial zirconium alloys, ASTM STP 1597 (2018) 796–822, doi:10.1520/stp159720160068.

[46] A. Baris, R. Restani, R. Grabherr, Y.-L. Chiu, H.E. Evans, K. Ammon, M. Limbäck, S. Abolhassani, Chemical and microstructural characterization of a 9 cycle Zircaloy-2 cladding using EPMA and FIB tomography, J. Nucl. Mater. 504 (2018) 144–160, doi:10.1016/j.jnucmat.2018.01.065.

[47] A. Baris, S. Abolhassani, R. Grabherr, R. Restani, R. Schäublin, Y.L. Chiu, H.E. Evans, K. Ammon, M. Limbäck, Causes of increased corrosion and hydrogen uptake of Zircaloy-2 cladding at high burnups – a comparative study of the chemical composition of a 3 cycle and a 9 cycle cladding, ENS TopFuel, Prague, Czech Republic (2018) A0172.

[48] G. Kuri, H. Ramanantoanina, J. Bertsch, M. Martin, I. Panas, Chemical state and atomic scale environment of nickel in the corrosion layer of irradiated Zircaloy-2 at a burn-up around 45 MWd/kg, Corros. Sci. 143 (2018) 200–211, doi:10.1016/j.corsci.2018.08.032.

[49] A.W. Colldeweih, A. Baris, P. Spätig, S. Abolhassani, Evaluation of mechanical properties of irradiated zirconium alloys in the vicinity of the metal-oxide interface, Mater. Sci. Eng. A 742 (2019) 842–850, doi:10.1016/j.msea.2018.09.107.

[50] J. Hawes, A. Baris, Y.-L. Chiu, S. Abolhassani, Characterization of the conductivity of metal-oxide interface of zirconium based fuel cladding at low and high burnups, J. Nucl. Mater. 534 (2020) 152133, doi:10.1016/j.jnucmat.2020.152133.

[51] T. Ungár, P. Frankel, G. Ribárik, C.P. Race, M. Preuss, Size-distribution of irradiation-induced dislocation-loops in materials used in the nuclear industry, J. Nucl. Mater. 550 (2021) 152945, doi:10.1016/j.jnucmat.2021.152945.

[52] T. Ungár, G. Ribárik, M. Topping, R.M.A. Jones, X.D. Xu, R. Hulse, A. Harte, G. Tichy, C.P. Race, P. Frankel, M. Preuss, Characterizing dislocation loops in irradiated polycrystalline Zr alloys by X-ray line profile analysis of powder diffraction patterns with satellites, J. Appl. Crystallogr. 54 (2021) 803–821, doi:10.1107/s1600576721002673.

[53] S. Abolhassani, A. Baris, R. Grabherr, J. Hawes, A. Colldeweih, R. Vanta, R. Restani, A. Hermann, J. Bertsch, M. Chollet, G. Kuri, M. Martin, S. Portier, H. Wiese, H. Schweikert, G. Bart, K. Ammon, G. Ledergerber, M. Limbäck, Toward an improved understanding of the mechanisms involved in the increased hydrogen uptake and corrosion at high burnups in zirconium based claddings, ASTM STP1622 (2021) 435–466, doi:10.1520/STP162220190052.

[54] L. Walters, S.R. Douglas, M. Griffiths, Equivalent radiation damage in zirconium irradiated in various reactors, ASTM STP 1597 (2018) 676–690, doi:10.1520/STP159720160101.

[55] K. Thompson, D. Lawrence, D.J. Larson, J.D. Olson, T.F. Kelly, B. Gorman, In situ site-specific specimen preparation for atom probe tomography, Ultramicroscopy 107 (2007) 131–139, doi:10.1016/j.ultramic.2006.06.008.

[56] D.R. Kingham, The post-ionization of field evaporated ions: a theoretical explanation of multiple charge states, Surf. Sci. 116 (1982) 273–301, doi:10.1016/0039-6028(82)90434-4.

[57] J.M. Hyde, C.A. English, An analysis of the structure of irradiation induced Cu-enriched clusters in low and high nickel welds, MRS Online Proc. Libr. 650 (2000) 66, doi:10.1557/PROC-650-R6.6.

[58] D. Vaumousse, A. Cerezo, P.J. Warren, A procedure for quantification of precipitate microstructures from three-dimensional atom probe data, Ultramicroscopy 95 (2003) 215–221, doi:10.1016/S0304-3991(02)00319-4.

[59] H.H. Shen, X.T. Zu, B. Chen, C.Q. Huang, K. Sun, Direct observation of hydrogenation and dehydrogenation of a zirconium alloy, J. Alloys Compd. 659 (2016) 23–30, doi:10.1016/j.jallcom.2015.11.031.

[60] S.M. Hanlon, S.Y. Persaud, F. Long, A. Korinek, M.R. Daymond, A solution to FIB induced artefact hydrides in Zr alloys, J. Nucl. Mater. 515 (2019) 122–134, doi:10.1016/j.jnucmat.2018.12.020.

[61] G. Sundell, M. Thuvander, H.-O. Andrén, Hydrogen analysis in APT: methods to control adsorption and dissociation of H_2, Ultramicroscopy 132 (2013) 285–289, doi:10.1016/j.ultramic.2013.01.007.

[62] I. Mouton, A.J. Breen, S. Wang, Y. Chang, A. Szczepaniak, P. Kontis, L.T. Stephenson, D. Raabe, M. Herbig, T.B. Britton, B. Gault, Quantification challenges for atom probe tomography of hydrogen and deuterium in Zircaloy-4, Microsc. Microanal. 25 (2019) 481–488, doi:10.1017/S143192761801615X.

[63] P. Tejland, H.-O. Andrén, Oxidation induced localized creep deformation in Zircaloy-2, J. Nucl. Mater. 444 (2014) 30–34, doi:10.1016/j.jnucmat.2013.09.020.

[64] P. Wang, J. Bowman, M. Bachhav, B. Kammenzind, R. Smith, J. Carter, A. Motta, E. Lacroix, G. Was, Emulation of neutron damage with proton irradiation and its effects on microstructure and microchemistry of Zircaloy-4, J. Nucl. Mater. 557 (2021) 153281, doi:10.1016/j.jnucmat.2021.153281.

[65] O.C. Hellman, J.A. Vandenbroucke, J. Rüsing, D. Isheim, D.N. Seidman, Analysis of three-dimensional atom-probe data by the proximity histogram, Microsc. Microanal. 6 (2000) 437–444, doi:10.1007/s100050010051.

[66] P. Rudling, K. Lundblad Vannesjö, G. Vesterlund, A.R. Massih, Influence of second-phase particles on Zircaloy corrosion in BWR environment, ASTM STP 939 (1987) 292–306, doi:10.1520/STP28128S.

[67] Y. Ito, T. Furuya, The effect of annealing parameter on corrosion resistance of Zircaloy-2, J. Nucl. Sci. Technol. 32 (1995) 1118–1126, doi:10.1080/18811248.1995.9731826.

[68] Z.D. Shah, Characterizing and Modelling Precipitation in Zirconium Alloys, University of Manchester, 2019 Ph.D. thesis.

[69] Z. Yu, M. Bachhav, F. Teng, L. He, A. Couet, Nanoscale redistribution of alloying elements in high-burnup AXIOM-2 (X2®) and their effects on in-reactor corrosion, Corros. Sci. 190 (2021) 109652, doi:10.1016/j.corsci.2021.109652.

[70] B. Gault, Y.M. Chen, M.P. Moody, T. Ohkubo, K. Hono, S.P. Ringer, Influence of the wavelength on the spatial resolution of pulsed-laser atom probe, J. Appl. Phys. 110 (2011), doi:10.1063/1.3657846.

[71] K. Lindgren, K. Stiller, P. Efsing, M. Thuvander, On the analysis of clustering in an irradiated low alloy reactor pressure vessel steel weld, Microsc. Microanal. 23 (2017) 376–384, doi:10.1017/S1431927617000162.

[72] G.M. Hood, Point defect diffusion in α-Zr, J. Nucl. Mater. 159 (1988) 149–175, doi:10.1016/0022-3115(88)90091-8.

[73] J.F. March-Rico, G. Huang, B.D. Wirth, The effect of local chemical environment on the energetics of stacking faults and vacancy platelets in α-zirconium, J. Nucl. Mater. 540 (2020) 152339, doi:10.1016/j.jnucmat.2020.152339.

[74] A.J. Breen, I. Mouton, W. Lu, S. Wang, A. Szczepaniak, P. Kontis, L.T. Stephenson, Y. Chang, A.K. da Silva, C.H. Liebscher, D. Raabe, T.B. Britton, M. Herbig, B. Gault, Atomic scale analysis of grain boundary deuteride growth front in Zircaloy-4, Scr. Mater. 156 (2018) 42–46, doi:10.1016/j.scriptamat.2018.06.044.

[75] M. Christensen, W. Wolf, C.M. Freeman, E. Wimmer, R.B. Adamson, L. Hallstadius, P.E. Cantonwine, E.V. Mader, Effect of alloying elements on the properties of Zr and the Zr–H system, J. Nucl. Mater. 445 (2014) 241–250, doi:10.1016/j.jnucmat.2013.10.040.

[76] G. Sundell, M. Thuvander, H.-O. Andrén, Enrichment of Fe and Ni at metal and oxide grain boundaries in corroded Zircaloy-2, Corros. Sci. 65 (2012) 10–12, doi:10.1016/j.corsci.2012.08.061.

[77] T. Sawabe, T. Sonoda, S. Kitajima, T. Kameyama, Analysis of atomic distribution in as-fabricated Zircaloy-2 claddings by atom probe tomography under high-energy pulsed laser, J. Nucl. Mater. 442 (2013) 168–174, doi:10.1016/j.jnucmat.2013.08.048.

[78] A.T. Motta, L. Capolungo, L.-Q. Chen, M.N. Cinbiz, M.R. Daymond, D.A. Koss, E. Lacroix, G. Pastore, P.-C.A. Simon, M.R. Tonks, B.D. Wirth, M.A. Zikry, Hydrogen in zirconium alloys: a review, J. Nucl. Mater. 518 (2019) 440–460, doi:10.1016/j.jnucmat.2019.02.042.

[79] B.V. Cockeram, K.J. Leonard, L.L. Snead, M.K. Miller, The use of a laser-assisted Local Electrode Atom Probe and TEM to examine the microstructure of Zircaloy and precipitate structure following low dose neutron irradiation at nominally 358°C, J. Nucl. Mater. 433 (2013) 460–478, doi:10.1016/j.jnucmat.2012.10.006.

[80] C. Jones, V. Tuli, Z. Shah, M. Gass, P.A. Burr, M. Preuss, K.L. Moore, Evidence of hydrogen trapping at second phase particles in zirconium alloys, Sci. Rep. 11 (2021) 4370, doi:10.1038/s41598-021-83859-w.

[81] W. Lu, P. Kontis, S. Wang, R. Birch, M. Wenman, B. Gault, T.B. Britton, Nanoscale characterisation of hydrides and secondary phase particles in Zircaloy-4. Preprint 2021. https://export.arxiv.org/pdf/2109.10955. Accessed 07 October 2021.

[82] J. Liu, K. Li, J. Sayers, T. Aarholt, G. He, H. Hulme, A. Garner, M. Preuss, H. Nordin, J.M. Partezana, M. Limbäck, S. Lozano-Perez, S. Ortner, C.R.M. Grovenor, Characterisation of deuterium distributions in corroded zirconium alloys using high-resolution SIMS imaging, Acta Mater. 200 (2020) 581–596, doi:10.1016/j.actamat.2020.09.040.

[83] P.A. Burr, S.T. Murphy, S.C. Lumley, M.R. Wenman, R.W. Grimes, Hydrogen accommodation in Zr second phase particles: implications for H pick-up and hydriding of Zircaloy-2 and Zircaloy-4, Corros. Sci. 69 (2013) 1–4, doi:10.1016/j.corsci.2012.11.036.

[84] W. Yeniscavich, R.A. Wolfe, R.M. Lieberman, Hydrogen absorption by nickel enriched Zircaloy-2, J. Nucl. Mater. 1 (1959) 271–280, doi:10.1016/0022-3115(59)90023-6.

[85] M. Lindgren, G. Sundell, I. Panas, L. Hallstadius, M. Thuvander, H.-O. Andrén, Toward a comprehensive mechanistic understanding of hydrogen uptake in zirconium alloys by combining atom probe analysis with electronic structure calculations, ASTM STP 1543 (2015) 515–539, doi:10.1520/stp154320120164.